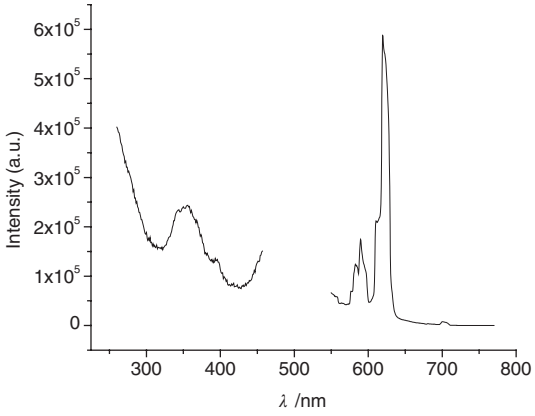

Fig. 5. Excitation and emission spectrum of Eu^{3+} doped Y_2O_2S nanotubes.

duced by the electron transition from $^5D_0$ to $^7F_1$ levels) and the other at 621 nm (produced by the electron transition from $^5D_0$ to $^7F_4$ levels).[9] A strong up-conversion emission under light from ordinary Xe sources (excitation wavelength: 980 nm) has been observed (Fig. 6) in the Yb^{3+} and Er^{3+} co-doped Y_2O_2S nanotubes with emission bands centered at

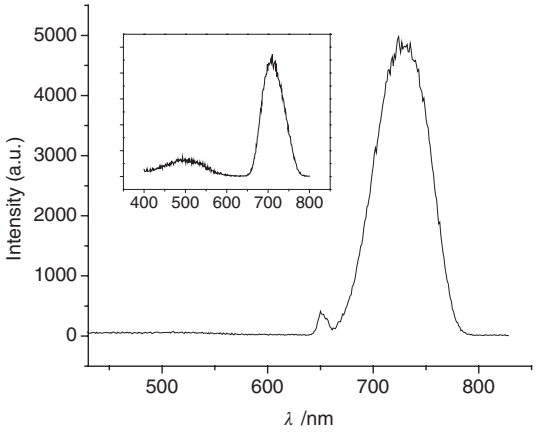

Fig. 6. Up-conversion spectrum of Yb^{3+}/Er^{3+} Co-doped Y_2O_2S nanotubes (Xe sources, 980 nm). Inset: down-conversion spectrum of Yb^{3+}/Er^{3+} co-doped Y_2O_2S nanotubes (Xe light source, 310 nm).

650 nm (due to the electron transition from $^4F_{9/2}$ to $^4I_{15/2}$ levels) and 730 nm (due to the electron transition from $^4I_{9/2}$ to $^4I_{15/2}$ levels, see Supporting materials). This coincides well with the down conversion emission (two bands, 500 nm and 730 nm) of these nanotubes when excited with 300, 310, or 320 nm Xe light sources.[10] The excellent luminescent properties of these functionalized nanotubes may find applications such as biological labels[11–14] or optoelectronic and nanodevices.[15–17] Meanwhile, we believe this chemical modification method to rare earth compound nanotubes could be widely applied in many other fields, especially for catalysts.

The above studies illustrate the potential of our approach for the synthesis and functionalization of rare earth compound nanotubes. Based on these methods, other kinds of rare earth compound or composite nanotubes and nanotube-related structures, such as oxybromides, oxychlorides, oxide–halide composite nanotubes, nanotube–nanorods composites, nanotube–nanorods heterojunctions, and so on, could be easily obtained and functionalized. We believe that, as an ideal combination of multifunctional compounds and particular tubular structures, these nanotubes and nanotube-related structures will find applications in optoelectronic and nanoscale devices, low dimensional physics and material science, biological technology, and molecular catalysts.

Experimental

Synthesis of Rare Earth Hydroxide Nanotubes: In a typical synthesis, 0.5 g of rare earth oxides (Y_2O_3, La_2O_3, Pr_2O_3, Nd_2O_3, Sm_2O_3, Eu_2O_3, Gd_2O_3, Th_2O_3, Dy_2O_3, Ho_2O_3, Er_2O_3, Tm_2O_3, Yb_2O_3) were dissolved by 10 % diluted nitric acid to form clear aqueous solution, then 10 % KOH (or NaOH) solution was added to adjust the system to ~ pH 2–14. The as-obtained colloidal precipitate was transferred into a 40 mL autoclave, sealed and kept at ~ 120–140 °C for ~ 12–24 hr. After that, the autoclave was allowed to cool to room temperature naturally. The precipitate was then filtered, washed with water to remove ions possibly remnant in the final products, and dried at 80 °C in air. Following the above procedure, all of the mentioned rare earth hydroxide nanotubes could be obtained.

Received: March 26, 2003
Final version: May 25, 2003

[1] S. Iijima, *Nature* **1991**, *354*, 56.
[2] R. Tenne, L. Margulis, M. Genut, G. Hodes, *Nature* **1992**, *360*, 444.
[3] Y. Feldman, E. Wasserman, D. J. Srolovitz, R. Tenne, *Science* **1995**, *267*, 222.
[4] Y. R. Hacohen, E. Grunbaum, R. Tenne, J. Sloan, J. L. Hutchison, *Nature* **1998**, *395*, 336.
[5] N. G. Chopra, R. J. Luyken, K. Cherrey, V. H. Crespi, M. L. Cohen, S. G. Louie, A. Zettl, *Science* **1995**, *269*, 966.
[6] M. E. Spahr, P. Bitterli, R. Nesper, M. Müller, F. Krumeich, H. U. Nissen, *Angew. Chem. Int. Ed.* **1998**, *37*, 1263.
[7] Y. D. Li, J. W. Wang, Z. X. Deng, Y. Y. Wu, X. M. Sun, D. P. Yu, P. D. Yang, *J. Am. Chem. Soc.* **2001**, *123*, 9904.
[8] X. Wang, Y. D. Li, *Angew. Chem. Int. Ed.* **2002**, *41*, 4790.
[9] M. Tanaka, G. Nishimura, T. Kushida, *Phys. Rev. B* **1994**, *49*, 16 917.
[10] L. Laversenne, S. Kairouani, Y. Guyot, C. Goutaudier, G. Boulon, M. T. Cohen-Adad, *Opt. Mater.* **2002**, *19*, 59.
[11] W. C. W. Chan, S. M. Nie, *Science* **1998**, *281*, 2016.
[12] W. C. W. Chan, D. J. Maxwell, X. H. Gao, R. E. Bailey, M. Y. Han, S. M. Nie, *Curr. Opin. Biotech.* **2002**, *13*, 40.
[13] M. Y. Han, X. H. Gao, J. Z. Su, S. M. Nie, *Nat. Biotechnol.* **2001**, *19*, 631.
[14] M. Bruchez, M. Moronne, P. Gin, S. Weiss, A. P. Alivisatos, *Science* **1998**, *281*, 2013.
[15] X. F. Duan, Y. Huang, Y. Cui, J. F. Wang, C. M. Lieber, *Nature* **2001**, *409*, 66.
[16] J. F. Wang, M. S. Gudiksen, X. F. Duan, Y. Cui, C. M. Lieber, *Science* **2001**, *293*, 1455.
[17] M. H. Huang, S. Mao, H. Feick, H. Q. Yan, Y. Y. Wu, H. Kind, E. Weber, R. Russo, P. D. Yang, *Science* **2001**, *292*, 1897.

Rectangular Single-Crystal Mullite Microtubes

By *Xiang Y. Kong*, *Zhong L. Wang*,* and *Jiansheng Wu*

Tubular structures on the micro- and nano-scale have attracted extensive interest over the past decade due to their great potential for studying space-confined transport phenom-

[*] Prof. Z. L. Wang, Dr. X. Y. Kong
School of Materials Science and Engineering
Georgia Institute of Technology
Atlanta, GA 30332-0245 (USA)
E-mail: zhong.wang@mse.gatech.edu
Dr. X. Y. Kong, Prof. J. Wu
School of Materials Sciences and Engineering
Shanghai Jiao Tong University
Huashan Road 1954, Shanghai 200030 (P.R. China)

 DOI: 10.1002/adma.200305405

ADVANCED MATERIALS

ena and applications in nanotechnology. As inspired by the structure of carbon nanotubes,[1] tubular structures have been fabricated for compounds with layered structures such as MoS_2[2] and BN.[3] Using nanotubes, nanobelts,[4] and nanowires as templates, tubular structures have also been synthesized for a range of materials that do not have a layered structure.[5–12] Most of the tubes have cylindrical symmetry, however, some are amorphous, polycrystalline, or textured nanocrystal films. As a result of the strong drive towards applications in nanoelectronics and nanooptoelectronics, as well as catalysis, research has been mainly devoted to synthesizing smaller-sized nanotubes ranging from a few nanometers to a few tens of nanometers. The nanotubes usually have a uniform exterior wall structure with a small interior that is sometimes partially or completely blocked by growth products. Hence, the inner walls and the cavity channels are less useful than the exterior walls. For applications in biomedical drug delivery,[13] biochips, and microfluidic processes in microelectromechanical systems (MEMS),[14] it is desirable to have microtubes in the size range of a few micrometers with high mechanical strength and chemical robustness, which will be effective for penetrating biological tissue and transporting fluid. Here we report a novel single-crystalline microtubular structure of aluminum-rich mullite, $Al_2(Al_{2+2x}Si_{2-2x})O_{10-\delta}$ ($x \sim 0.375$) which has a perfect rectangularly framed cross-section with specific crystallographic facets, a large hollow interior channel of 0.5–3 μm width, and thin walls (50–100 nm). The ceramic microtubes are mechanically hard with potential applications as hollow needles for drug delivery, microchannels for MEMS/biochips, and as optical resonance cavities and waveguides.

Mullite ceramics are known as superior engineering materials due to their excellent mechanical, electronic, and optical properties.[15] Mullite whiskers, an important component in reinforced composites, have been synthesized via a fluoride catalyst assisted solid–vapor reaction.[16] The Al-rich mullite tubular structure reported here was synthesized using tungsten-comprising precursors. The overall surface of the substrate is covered by uniformly distributed hollow tubular structures with open ends (Fig. 1a). The widths of the tubes vary between 0.5–3 μm, but their lengths can be in the range of tens to even hundreds of micrometers. A scanning electron microscopy (SEM) image at a higher magnification clearly indicates that the wall thickness of the tubes is 50–100 nm (Fig. 1b). The sharp knife-shaped edges and tips are useful for penetrating biological tissues. The microtubes have square-framed (Fig. 1d) and rectangularly framed cross-sections (Figs. 1c,d). The tubes have a uniform, completely hollow structure without filling or blockage, which is an ideal structure for transporting fluid or gas at micro- to nano-scale. In some areas, tungsten rich oxide particles on the surfaces of the tubes have also been found, as indicated by the arrowhead in Figure 1c.

To avoid the complication introduced by the alumina substrate in energy dispersive X-ray spectroscopy (EDS) data quantification, our analysis was carried out by transmission

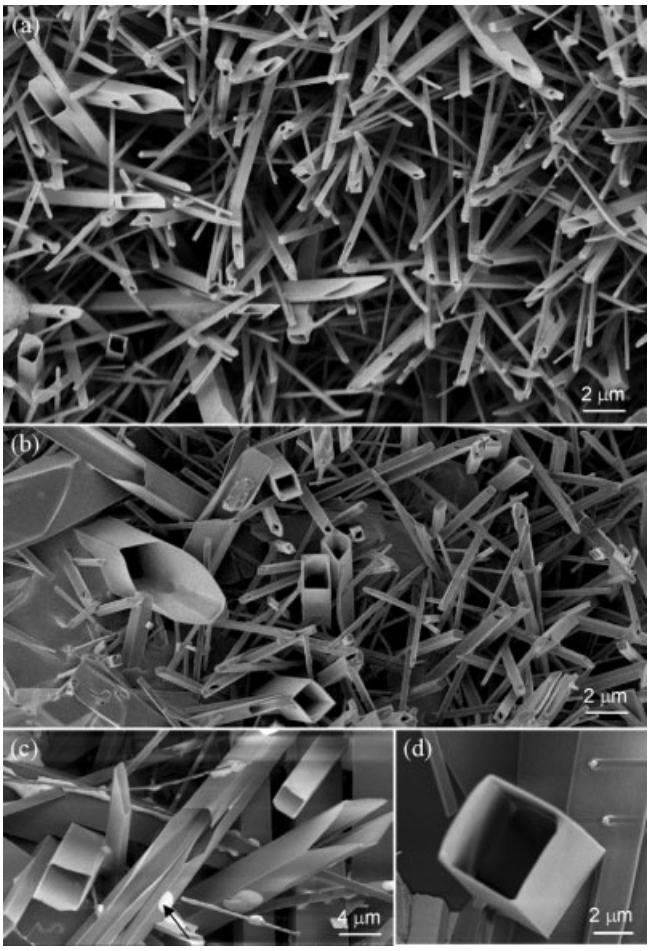

Fig. 1. SEM images of mullite single-crystal microtubes synthesized via the solid–vapor process, showing various structural and fracture configurations of the rectangular microtubes. The tube surface is flat and the wall thickness is uniform.

electron microscopy (TEM) so that the chemical information from individual microtubes could be obtained. Among approximately 100 individual tubes that were analyzed, the most common chemical composition is Al/Si ~ 3.8:1.0, with no detectable tungsten found in the tubes (the detection limit is ~ 2 at.-%). The closest chemical composition is $Al_{4.75}Si_{1.25}O_{10-\delta}$, which has an orthorhombic structure, the space group *Pbam*, and the following lattice parameters: $a = 0.7581$ nm, $b = 0.7686$ nm, and $c = 0.2887$ nm.[17]

The as-synthesized tubes were placed on a carbon-coated copper grid for TEM analysis. Figure 2 shows the results obtained from the same microtube under two different orientations. By tilting the microtube with its side-surface parallel to the electron beam, the bright-field and the corresponding dark-field TEM images unambiguously show the tubular structure. The corresponding electron diffraction pattern fits the $[1\bar{1}0]$ zone of $Al_{4.75}Si_{1.25}O_{10-\delta}$ (Fig. 2c), suggesting that the tube's top and bottom surfaces are $(1\bar{1}0)$ planes, the side surfaces are (110) planes, and the growth direction along the tube axis is in the [001] plane. To verify the crystallographic structure of the microtube, we kept the (001) spot in the dif-

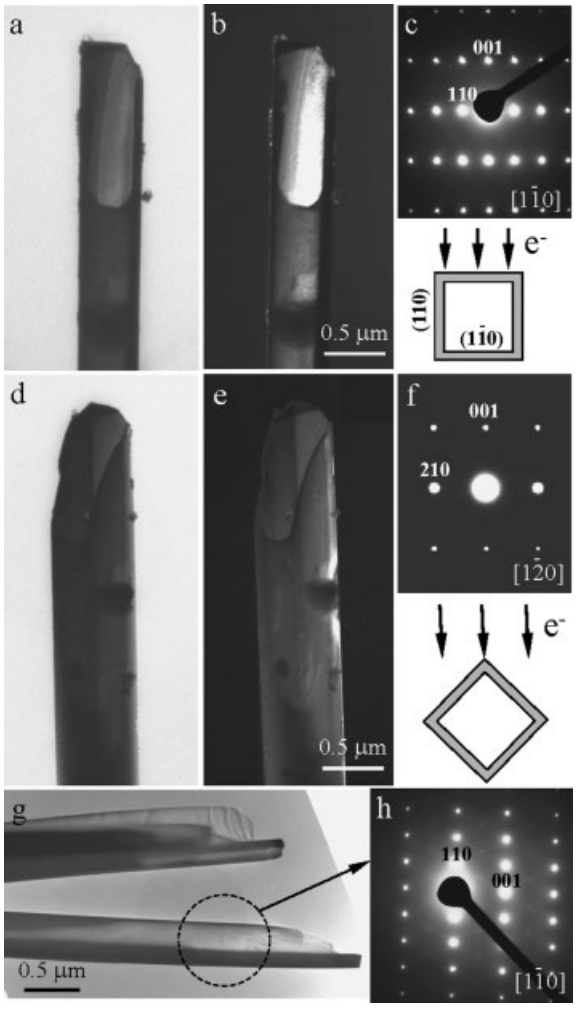

Fig. 2. a–c) Bright-field, dark-field TEM images, and the corresponding electron diffraction pattern, respectively, from a microtube oriented with the incident electron beam (e^-) perpendicular to the top surface. A schematic model of the microtube structure and orientation is inserted in (c). The dark-field image was recorded using the (110) diffracted beam. d–f) Bright-field, dark-field TEM images, and the corresponding electron diffraction pattern, respectively, recorded from the same microtube after being tilted through an angle such that the incident electron beam struck the microtube in the diagonal orientation across the cross-section. g,h) Bright-field TEM image and the corresponding electron diffraction pattern, respectively, recorded from other fractured microtubes, showing the [001] growth direction.

fraction pattern and tilted the microtube around its [001] symmetry axis to reach the [1$\bar{2}$0] zone axis. Such a careful operation is essential to ensure that the incident electron beam is perpendicular to the axis of the microtube and thus enable correct determination of its shape. Again, the bright-field and the corresponding dark-field TEM images unambiguously prove the tubular structure (Figs. 2d,e). The diagonal direction of the cross-section is the [210] plane (Fig. 2f). Electron image and diffraction pattern recorded from other microtubes (Figs. 2g,h) show consistent results.

The microtubes have a dislocation-free wall structure. High-resolution TEM images recorded along the [1$\bar{1}$0] plane, the normal direction of the top surface, show a clear and sharp lattice structure (Fig. 3a). The image was recorded from a thin section at the open end of the microtube. The (110) and (001) lattice spacings match the expected structure of $Al_{4.75}Si_{1.25}O_{10-\delta}$ very well. The microtube shows no dislocation or planar defects in either the high-resolution TEM images or the low magnification TEM images. The contrast variation from top to bottom in Figure 3a is due to a change in the projected specimen thickness near the fracture edge. The (110) side surface shows atomic sharpness without any contamination. EDS analysis shows the presence of oxygen, Al and Si in the microtube (Fig. 3c), with an atomic ratio of Al/Si ~ 3.8:1.0.

High-resolution TEM imaging of the microtubes is sometimes limited by the thickness of the specimen. To avoid this problem, the microtube was tilted so that a thin projected corner of the tube is imaged in profile. Such a case is shown in Figure 3b, where the incident electron beam is along the [1$\bar{2}$2] plane, which is closely perpendicular to the microtube. A detailed examination of the image over a distance of 4 μm recorded on a single TEM image shows no dislocation. A small section of the image is displayed in Figure 3d where the (011) and (210) lattice fringes are clearly resolved. The projected corner is straight and atomically sharp.

Mullite is a unique family of oxide structures and has important applications in electronics and optics.[15] The structures of mullite and its derivatives have been extensively investigated.[18–21] Mullite belongs to the aluminum silicate family with an orthorhombic structure. The common formula for aluminum silicate is $Al_2(Al_{2+2x}Si_{2-2x})O_{10-\delta}$. The mullite crystal structure consists of a three-dimensional framework of alternate corner-sharing among the AlO_6 octahedra and the SiO_4 (or AlO_4) tetrahedra. The aluminum silicate crystal structure can be modified into various orthorhombic structures, ranging from sillimanite $Al_2O_3{\cdot}SiO_2$ to $4Al_2O_3{\cdot}SiO_2$ achieved by substituting Si^{4+} ions with Al^{3+} ions in the tetrahedral sites of the alternating aluminum and silicon columns and the introduction of ordered oxygen vacancies.

Based on the crystal lattice model for $Al_{4.75}Si_{1.25}O_{10-\delta}$ (Fig. 4a), the model for the top and side surfaces {110} planes of the microtubes is given in Figure 4b. The white box indicates the unit cell of the projected cation atoms in correspondence to the structure observed in the high-resolution TEM image in Figure 3a. The model for the growth front is given in Figure 4c.

The mullite microtubes have several unique features. Firstly, the shape and crystallographic facet structure are controlled and well defined; their surfaces are atomically flat. Secondly, every microtube is a single crystal without the presence of line or planar defects, indicating superior mechanical hardness and strength. Thirdly, the microtube has a completely hollow interior, open ends, and thin walls; thus, it is sharp and may be effective in penetrating biological tissue. Fourthly, the mullite is a ceramic material; hence, it exhibits the typical characteristics of a ceramics—high hardness, strong, resistance to corrosion and oxidation, and resilience to high temperatures.[22] Finally, the synthesis process we developed produces the tubular structure at high yield. The process is cheap, allowing the possibility of large-scale production.

ADVANCED MATERIALS

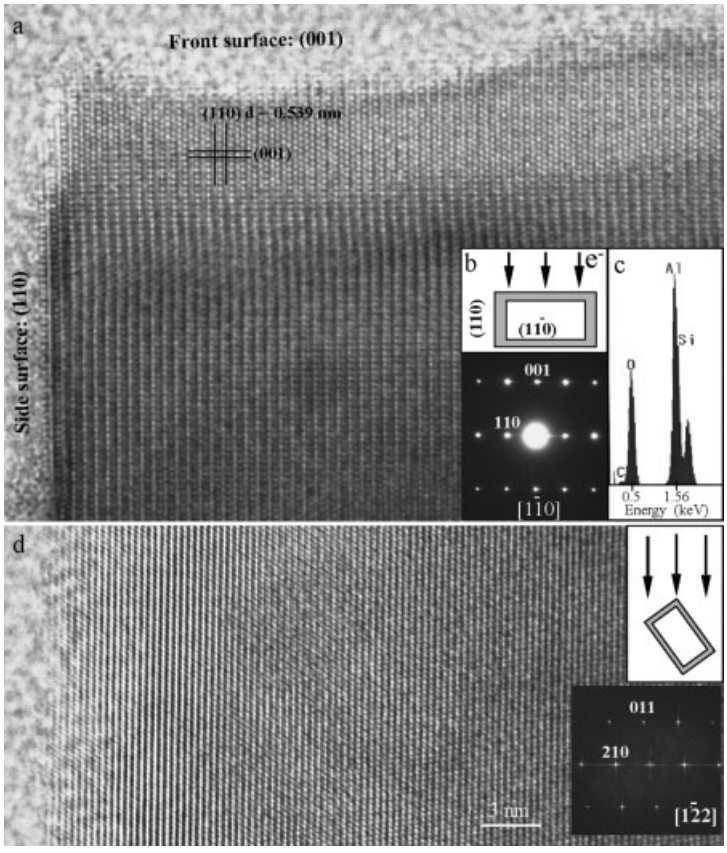

Fig. 3. a) High-resolution TEM image recorded from a thin edge near the growth front of a microtube, oriented along the [1$\bar{1}$0] plane. b) The corresponding electron diffraction pattern from the region and a schematic of the incident geometry of the electron beam. c) EDS spectrum acquired from the microtube showing the presence of O, Al and Si in the structure. d) High-resolution TEM image recorded from the side edge of a microtube, oriented along the [1$\bar{2}$2] plane. A Fourier transform of the image is inserted, and the corresponding imaging geometry is also given.

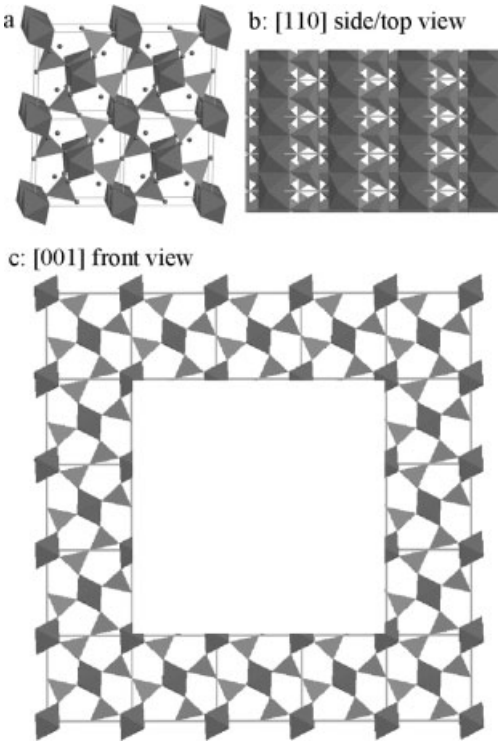

Fig. 4. a) Unit cell model of mullite ($Al_{4.75}Si_{1.25}O_{10-\delta}$), where the tetrahedrally coordinated Si (or Al), octahedrally coordinated Al, and the oxygen located at the corners of the polyhedra are shown. b) The [110] or [1$\bar{1}$0] projected structure of the unit cell, which represents the top/side surface of the microtube. c) Front view of the microtube structure.

The microtubes are also interesting from the crystal growth point of view. Our microscopy analysis found no catalyst particles at the ends of the microtubes and the tungsten content is below the detection limit. Hence, the nucleation and growth of the single-crystalline, rectangularly framed microtubes on a polycrystalline alumina substrate would require systematic and extensive study. However the unique structure and geometric shape as well as superior properties of the mullite microtubes could have an impact on the applications in a number of fields. Micro-needles based on silicon have previously been fabricated for drug delivery,[23] but these needles are solid. The hollow-structured mullite microtubes with high mechanical strength and hardness may have high penetrability through biological tissues for drug delivery. The microtubes may also be used for injection or extraction of biofluids to and from small biological cells, giving the possibility of delivering, manipulating, and engineering genes. An important component in MEMS systems and biochips is the microchannels for fluid. The mullite microtubes could be useful for transporting fluid/gas at micro- to nano-scale. As the size of these mullite microtubes is compatible to the wavelengths of visible light, they may also be useful as optical resonance cavities and waveguides. In addition, the hollow structure of the tubules may serve as a mode for aligning nanowires for nanoelectronics,[24] as a template for synthesis of other nanostructures, and as a component of high performance composites.

Experimental

The Al-rich mullite tubular structure reported here was synthesized using tungsten-comprising precursors, which has been demonstrated to be the key component for the formation of the tubular structure [25]. Commercially available aluminum chloride ($AlCl_3$) and tetraethoxysilane (TEOS) were used as the source materials for making the gel precursor. Ammonium *meta*-tungstate hydrate was employed as a catalyst. The relative molar composition of the source materials was $AlCl_3$/TEOS/catalyst/H_2O = 4:1:0.25:120. These source solutions and the catalyst were mixed and stirred at 60 °C for 4 h; a creamy white–green gel resulted. The gel precursor was spun onto a polycrystalline alumina substrate forming a uniform coating, and baked at 250 °C overnight. The alumina plates were placed into a horizontal tube furnace kept at a constant pressure of 400 torr and the furnace was heated at a rate of ~ 20 °C min^{-1} up to 1180 °C. The reaction was kept at 1180 °C for 6 h and then cooled slowly to room temperature. The mullite tubular structures were formed with high yield on the alumina substrate. This experiment has extraordinary repeatability. The collected product was characterized by SEM (LEO1530 FEG apparatus at 5 kV), high-resolution TEM (Hitachi HF-2000 FEG apparatus at 200 kV and JEOL 4000EX high resolution TEM at 400 kV), and EDS.

Received: May 15, 2003
Final version: June 11, 2003

[1] S. Iijima, *Nature* **1991**, *354*, 56.
[2] M. Remskar, A. Mrzel, Z. Skraba, A. Jesih, M. Ceh, J. Demsar, P. Stadelmann, F. Levy, D. Mihailovic, *Science* **2001**, *292*, 479.
[3] N. G. Chopra, R. J. Luyken, K. Cherrey, V. H. Crespi, M. L. Cohen, S. G. Louie, A. Zettl, *Science* **1995**, *269*, 966.
[4] Z. W. Pan, Z. R. Dai, Z. L. Wang, *Science* **2001**, *291*, 1947.
[5] Z. L. Wang, R. P. Gao, J. L. Gole, J. D. Stout, *Adv. Mater.* **2000**, *12*, 1938.
[6] C. R. Martin, *Science* **1994**, *266*, 1961.
[7] B. C. Satishkumar, A. Govindaraj, E. M. Vogl, L. Basumallick, C. N. R. Rao, *J. Mater. Res.* **1997**, *12*, 604.
[8] X. D. Wang, P. X. Gao, J. Li, C. J. Summers, Z. L. Wang, *Adv. Mater.* **2002**, *14*, 1732.
[9] J. Goldberger, R. R.He, Y. F. Zhang, S. W. Lee, H. Q. Yan, H. J. Choi, P. D. Yang, *Nature* **2003**, *422*, 599.
[10] G. R. Patzke, F. Krumeich, R. Nesper, *Angew. Chem. Int. Ed.* **2002**, *41*, 2446.
[11] P. M. Ajayan, O. Stephan, P. Redlich, C. Colliex, *Nature* **1995**, *375*, 564.
[12] P. Hoyer, *Langmuir* **1996**, *12*, 1411.
[13] J. T. Santini, M. J. Cima, R. Langer, *Nature* **1999**, *397*, 335.
[14] T. Thorsen, S. J. Maerkl, S. R. Quake, *Science* **2002**, *298*, 580.
[15] I. A. Aksay, D. M. Aabbs, M. Sarikaya, *J. Am. Ceram. Soc.* **1991**, *74*, 2343.
[16] K. Okada, N. Otuska, *J. Am. Ceram. Soc.* **1991**, *74*, 2414.
[17] T. Ban, K. Okada, *J. Am. Ceram. Soc.* **1992**, *75*, 227.
[18] R. J. Angel, C. T. Prewitt, *Am. Mineral.* **1986**, *71*, 1476.
[19] R. J. Angel, R. K. Mcmullan, C. T. Prewitt, *Am. Mineral.* **1991**, *76*, 332.
[20] R. X. Fischer, H. Schneider, M. Schmucker, *Am. Mineral.* **1994**, *79*, 983.
[21] S. H. Rahman, H. T. Weichert, *Acta Crystallogr., Sect. B: Struct. Sci.* **1990**, *46*, 139.
[22] Mullite has a hardness of 10.7 GPa, an elastic modulus of 151 GPa, a thermal conductivity of 6 W mK^{-1}, and a dielectric constant of 5.8 @ 1 MHz.
[23] D. V. McAllister, M. G. Allen, M. R. Prausnitz, *Annu. Rev. Biomed. Eng.* **2000**, *2*, 289.
[24] Y. Huang, X. F. Duan, Q. Q. Wei, C. M. Lieber, *Science* **2001**, *291*, 630.
[25] X. Y. Kong, Z. L. Wang, patent pending.

Micropatterning of Metal Nanoparticles via UV Photolithography**

By *Shin Horiuchi*,* *Takashi Fujita*, *Teruaki Hayakawa* and *Yukimichi Nakao*

The assembly and fabrication of two- or three-dimensional (2D or 3D) micro- and nanoscale structures using metal nanoparticles as building blocks is a very promising technique for the creation of next generation electronic, opto-electronic and chemical sensing devices.[1,2] Polymer/metal nanoparticle hybrid systems having a well defined pattern of metal nanoparticles in 2D and 3D are expected to have variety of applications as lithographic masks,[3–6] photonic bandgap materials,[7,8] high storage devices,[9] or catalysts.[10–12]

We have developed a simple dry process to arrange metal nanoparticles using block copolymer films.[13,14] This process uses a one step synthesis.[15] Vapor of palladium(II) bis(acetylacetonato), ($Pd(acac)_2$) (Note: acac denotes $CH_3COCHCOCH_3$), is exposed to a polymer film in a nitrogen atmosphere at 180 °C for periods of up to 2 h. $Pd(acac)_2$ is sublimed at atmospheric pressure, and the vapor penetrates into the polymer film. The metal complex decomposes and is reduced into the metallic state, forming nanoparticles. The reducing power of polymers varies; for example, polystyrene (PS) reduces faster than polymethylmethacrylate (PMMA). Therefore, in block copolymer films of polystyrene-*b*-polymethylmethacrylate (PS-*b*-PMMA), the metal complex is selectively reduced in the PS phase. As a result, the metal nanoparticles are arranged in patterns that reflect the underlying morphologies of the block copolymers. We evaluated the reduction of $Pd(acac)_2$ and the formation of Pd nanoparticles in various types of polymers. PMMA showed a unique behavior with respect to the absorption and reduction of Pd $(acac)_2$.[13,14] That is, all the evaluated polymers except PMMA absorb and reduce $Pd(acac)_2$ simultaneously. On the other hand, for PMMA there is an induction period between the absorption and the reduction of $Pd(acac)_2$. This means that PMMA possesses a unique character that delays the formation of metal nanoparticles.

In this communication, we report on the possibility of patterning metal nanoparticles by way of conventional UV photolithography using the unique behavior of PMMA in terms

[*] Dr. S. Horiuchi, Dr. T. Fujita
Research Center of Macromolecular Technology
National Institute of Advanced Industrial Science and Technology
Tokyo WaterFront, 2-41-6, Aomi, Kohtoh-ku, 135-0064 Tokyo (Japan)
E-mail: s.horiuchi@aist.go.jp
Dr. T. Hayakawa
Research Center of Macromolecular Technology
National Institute of Advanced Industrial Science and Technology
Tsukuba Central 5, 1-1-1, Higashi, Tsukuba, 305-8565 Ibaraki (Japan)
Dr. Y. Nakao
Nanotechnology Research Institute
National Institute of Advanced Industrial Science and Technology
Tsukuba Central 5, 1-1-1, Higashi, Tsukuba, 305-8565 Ibaraki (Japan)

[**] We thank the financial support of New Energy and Industrial Technology Development (NEDO) for the Nanostructured Polymer Project.

 DOI: 10.1002/adma.200305270